

Imprinting electrically switchable scalar spin chirality by anisotropic strain in a Kagome antiferromagnet

Debjoty Paul,^{1,*} Shivesh Yadav,^{1,*} Shikhar Gupta,¹ Bikash Patra,¹ Nilesh Kulkarni,¹
 Debashis Mondal,¹ Kaushal Gavankar,¹ Saheli Samanta,¹ Sourav K. Sahu,^{1,2}
 Biswarup Satpati,³ Bahadur Singh,¹ Owen Benton,⁴ and Shouvik Chatterjee^{1,†}

¹*Department of Condensed Matter Physics and Materials Science,
 Tata Institute of Fundamental Research, Homi Bhabha Road, Mumbai 400005, India*

²*School of Physical Sciences, National Institute of Science Education and Research,
 An OCC of Homi Bhabha National Institute, Jatni 752050, India*

³*Surface Physics & Material Science Division, Saha Institute of Nuclear Physics,
 A CI of Homi Bhabha National Institute, 1/AF Bidhannagar, Kolkata 700064, India*

⁴*School of Physical and Chemical Sciences, Queen Mary University of London, London E1 4NS, United Kingdom*

Applying strain to epitaxial thin films has proven to be an effective approach for controlling material properties, paving the way for “materials by design”. In this study, we explore this concept in the context of topological Kagome antiferromagnets, which can exhibit a range of exotic magnetic states. One such material, Mn_3Sn , features a non-collinear yet coplanar inverse triangular spin order that lacks scalar spin chirality. By applying anisotropic strain to reduce the point group symmetry of the Kagome triangles from C_{3v} to C_1 , and utilizing the Dzyaloshinskii-Moriya interaction in epitaxial Mn_3Sn heterostructures, we achieve a canting of the manganese spins out of the Kagome plane. This newly induced magnetic state introduces a finite scalar spin chirality and results in a significant Berry phase in momentum space. Consequently, a large anomalous Hall effect emerges in the Kagome plane at room temperature, which can be fully controlled by charge current, enabling the realization of multiple-stable antiferromagnetic memory states.

I. INTRODUCTION

A Kagome lattice consists of corner sharing triangles, where a delicate interplay between geometrical frustration, magneto-crystalline anisotropies, and competing interactions can give rise to unconventional magnetic ground states [1, 2]. It can also host a non-trivial band structure in the momentum space, which is often intertwined with the magnetic order [3–5]. One such compound is Mn_3Sn that has been reported to have time-reversal symmetry breaking Weyl points [6–9]. Mn_3Sn has a hexagonal Ni_3Sn -type crystal structure (space group $P6_3/mmc$) that can be viewed as a bi-layer stacking of the Kagome planes along the c -axis/[0001] direction, as shown in Fig. 1a. The manganese (Mn) atoms form a two-dimensional Kagome lattice in the (0001)/ a - b plane with the tin (Sn) atoms at the centre of the hexagon. In the bulk, Mn_3Sn has a non-collinear inverse triangular spin structure over a wide temperature range between 50K and the Neel temperature of $T_N = 420\text{K}$ [10]. The Mn spins lie within the Kagome plane and rotate 120° anti-clockwise along a clockwise circulation of the Kagome triangle formed by the Mn atoms (see Fig. 1(a)) [11–13]. Magnetocrystalline anisotropy in Mn_3Sn cants the Mn spins slightly towards the Mn-Sn easy axis within the Kagome plane resulting in a small uncompensated moment [11, 12, 14, 15]. Al-

though magnetization is tiny, it shows a large anomalous Hall effect (AHE) at room temperature when the magnetic field is applied within the Kagome plane, which stems from intrinsic Berry curvature in the momentum space [16]. However, such a coplanar spin configuration preserves the combined symmetry TM_z , where T is the time reversal and M_z is the mirror symmetry with the (0001)/ a - b plane being the mirror plane, and the vertical glide symmetry $\tilde{M}_x = \{M_x|\frac{c}{2}\}$, where M_x is the mirror symmetry with the (1120)/ a - c plane being the mirror plane. This constrains Berry curvature (Ω_{xy}) to be $\Omega_{xy}(k_x, k_y, k_z) = -\Omega_{xy}(-k_x, -k_y, k_z)$. Accordingly, intrinsic Berry curvature contribution to the anomalous Hall conductivity (AHC) (σ_{xy}^z) in the Kagome (x - y) plane is identically zero, in accordance with experimental observation, both in single crystals and thin films [16–19].

Here, we show that anisotropic strain in combination with an in-plane Dzyaloshinskii-Moriya (DM) interaction arising from inversion symmetry breaking at thin film hetero-interfaces cants the Mn spins out of the Kagome plane resulting in a non-zero scalar spin chirality ($\chi = S_j \cdot (S_j \times S_k) \neq 0$) at room temperature. The out-of-plane spin canting also explicitly breaks the TM_z and \tilde{M}_x symmetries resulting in the appearance of finite Berry curvature in the Kagome plane (σ_{xy}^z). This gives rise to the observation of a large AHC (σ_{xy}^z) in the Kagome plane with the magnetic field applied along the c -axis [0001]. We further show that this anomalous Hall response can be completely switched at room temperature by the application of an electrical current pulse that induces a thermal assisted switching. Moreover, different domain configurations can be stabilized during the switching process that

*These authors contributed equally to this work.

†Authors to whom correspondence should be addressed: shouvik.chatterjee@tifr.res.in

allows realization of multiple-stable, non-volatile, anomalous Hall resistance (AHR) memory states.

II. RESULTS AND DISCUSSION

A. Anisotropic strain in epitaxial Mn₃Sn (0001) thin films

Epitaxial, (0001) out-of-plane oriented thin films of Mn₃Sn were fabricated by magnetron sputtering on *c*-plane sapphire substrates using tantalum (Ta), having the alpha (α) phase, as a buffer layer. Ta grows epitaxially on *c*-plane sapphire with Ta(110) planes oriented along the out-of-plane direction and having three domains in the in-plane direction that are rotated at 120 degrees from each other [20, 21]. This provides a quasi-six-fold symmetric template for epitaxial integration of Mn₃Sn(0001) thin films [22]. Epitaxial relationship in our thin films is Mn₃Sn (10 $\bar{1}$ 0)[0001]||Ta(100)[110]||Al₂O₃(11 $\bar{2}$ 0)[0001], determined from x-ray diffraction measurements. However, lattice mismatch between Ta and Mn₃Sn imparts an anisotropic tensile strain on Mn₃Sn atomic layers that we calculate by measuring the reciprocal lattice vectors (q_{\parallel} , q_z) of Mn₃Sn{20 $\bar{2}$ 1} family of diffraction spots, shown in Fig. 1(d) and Supplementary Information [22]. The anisotropic strain results in a reduction of the C_{3v} point group symmetry of the Kagome triangles to C_1 . The inter-atomic distances between the nearest neighboring Mn atoms in the Kagome triangle are now different, having the values of 2.845, 2.856, and 2.860Å, respectively, as shown in Fig. 1(a), in contrast to the uniform value of 2.838Å in the bulk [23]. The out-of-plane lattice parameter, $c = 4.538\text{\AA}$ in our thin films is similar to the reported value of 4.536Å in the bulk [23]. High-resolution transmission electron microscopy (HR-TEM) on these thin films also show similar lattice parameters [22]. The Mn₃Sn/Ta epitaxial heterostructures were capped with either AlO_x or Ta/AlO_x protective layers before exposing them to the ambient atmosphere.

Atomic layers of Ta has a strong spin-orbit coupling and breaks the inversion symmetry along the *c*-axis at the Mn₃Sn/Ta heterointerface. It, therefore, can stabilize a strong in-plane interfacial DM interaction [24–26] in the Mn₃Sn/Ta thin film heterostructures. The reduction of point group symmetry in Mn₃Sn due to anisotropic strain (see Fig. 1(a)) and in-plane DM interaction arising out of hetero-epitaxial interface plays an important role in stabilizing non-trivial magnetic ground state in these thin films, which will be discussed in the following sections. Ta also serves as an ideal buffer layer because it is stable against both Mn and Sn. This stability enables high-temperature annealing ($\geq 450^\circ\text{C}$) of Mn₃Sn, which is crucial for achieving epitaxial thin films with superior structural and electrical properties. This is in contrast to platinum (Pt), where interfacial reactions occur between Mn₃Sn and Pt at temperatures above 350°C [27]. Addi-

tional characterization of the thin film heterostructures can be found in the Supplementary Information [22].

B. Anomalous Hall effect in Mn₃Sn thin films with anisotropic strain

Having established the structural properties of the thin film heterostructures, we present their electrical and magnetic properties in Fig. 2. We observe a large AHC at room temperature when the measurements are done in the Kagome plane with the magnetic field applied perpendicular to it. This is in sharp contrast to the earlier reports on both bulk single crystals [16, 17] as well as epitaxial Mn₃Sn(0001) thin films [18, 19], where no AHC (σ_{xy}^z) is observed in the Kagome plane at room temperature. In those studies, no evidence for spontaneous magnetic moment was found when the magnetic field was applied perpendicular to the Kagome plane. This confirms that the co-planar spin configuration of Mn₃Sn, which preserves TM_z and \tilde{M}_x symmetries enforced σ_{xy}^z to be zero in those experiments. In our case, we observe a tiny magnetic moment, indicative of a finite canting of the Mn spins out of the Kagome plane. This induces finite scalar spin chirality and explicitly breaks the TM_z and \tilde{M}_x symmetries allowing the emergence of AHC (σ_{xy}^z), as observed in our measurements. The magnetic moment was found to be ≈ 9.3 and $16.5m\mu_B$ per Mn for 90nm thick Mn₃Sn films when capped with AlO_x (Ta(11nm)/Mn₃Sn(90nm)/AlO_x(8nm)) and Ta/AlO_x (Ta(11nm)/Mn₃Sn(90nm)/Ta(11nm)/AlO_x(8nm)), respectively, as shown in Fig. 2(c),(d). The corresponding AHCs are $\sigma_{xy}^z(H=0) \approx 27.7$ and $33.7(\Omega\text{-cm})^{-1}$, respectively (see Fig. 2(a),(b)). The carrier concentration in Mn₃Sn is estimated from the ordinary Hall effect, which is found to be similar in both kinds of heterostructures, $5.9 \times 10^{21}/\text{cc}$ and $6.1 \times 10^{21}/\text{cc}$ for the thin films capped with AlO_x and Ta/AlO_x, respectively. We note that the magnitudes of the AHC(σ_{xy}^z) in the Kagome plane of our thin films heterostructures are large, similar to what has been observed in bulk single crystals and thin films. However, in those cases AHC has only been observed in planes perpendicular to the Kagome plane. This, therefore, indicates a different magnetic ground state in our thin films compared to what has been reported before. Such a large AHC cannot be explained by the tiny magnetization (M_z), shown in Figs. 2(c),(d),[16] but points to a prominent role of scalar spin chirality and induced Berry curvature in the momentum space.

C. Anisotropic strain and in-plane Dzyaloshinskii-Moriya interaction induces scalar spin chirality in Mn₃Sn

To understand how out-of-plane spin canting is stabilized in Mn₃Sn/Ta heterostructures, we evaluate the ordered magnetic ground state of the Kagome lattice, which

respects all the relevant symmetries. The spin configuration in Mn_3Sn can be described by a Hamiltonian, which can be written as a sum over all Kagome triangles

$$H = \sum_{\Delta} H_{\Delta} \quad (1)$$

where

$$H_{\Delta} = (J\mathbf{S}_0 \cdot \mathbf{S}_1 + \mathbf{D}_{01} \cdot (\mathbf{S}_0 \times \mathbf{S}_1)) + (J\mathbf{S}_1 \cdot \mathbf{S}_2 + \mathbf{D}_{12} \cdot (\mathbf{S}_1 \times \mathbf{S}_2)) + (J\mathbf{S}_2 \cdot \mathbf{S}_0 + \mathbf{D}_{20} \cdot (\mathbf{S}_2 \times \mathbf{S}_0)) + \frac{1}{2} \sum_i K(\hat{\mathbf{n}}_i \cdot \mathbf{S}_i)^2 \quad (2)$$

where J , \mathbf{D}_{ij} , and K are the Heisenberg exchange, DM interaction, and easy-axis single ion anisotropy, respectively, where the local easy axis $\hat{\mathbf{n}}_i$ is oriented from site i to the center of the Kagome hexagons. The factor $\frac{1}{2}$ on the single-ion term is included to account for double counting when the total energy of the lattice is calculated by summing over all Kagome triangles. There is a hierarchy in the energy scale: $J > D > K$, which is typical for $3d$ transition metal ions such as Mn [28]. S_i , $i \in 0, 1, 2$ denotes the Mn spins on three Mn sublattices in Mn_3Sn , as shown in Fig. 3(b). In the absence of strain all Mn-Mn bonds in the Kagome triangles are of same length and related to each other by C_3 rotation symmetry (Fig. 1(a)). Therefore, the Heisenberg exchange interaction is expected to be of identical strength for each of the three bonds, $J_{ij} = J\mathcal{V}\langle i, j \rangle$, as used in eqn. 2. The symmetry allowed DM interaction, \mathbf{D}_{ij} , can be written as $\mathbf{D}_{ij} = D_z \hat{\mathbf{z}} + D_{\parallel} (\hat{\mathbf{z}} \times \hat{\mathbf{e}}_{ij})$, where $\hat{\mathbf{e}}_{ij}$ is the unit vector oriented from site i to site j . In the bulk, reflection symmetry of the Kagome planes forces D_{\parallel} to be identically zero. However, in $\text{Mn}_3\text{Sn}/\text{Ta}$ heterostructures, the hetero-epitaxial interface breaks the inversion symmetry along (0001) and hence, interfacial DM interaction can have a non-zero D_{\parallel} component. Following ref. [28] we set $\frac{D_z}{J}$ and $\frac{K}{J}$ as 0.1 and -0.03, respectively (note the different sign convention for $\frac{K}{J}$). For experimentally feasible values of $\frac{D_{\parallel}}{J}$ ($\frac{D_{\parallel}}{J} \leq \pm 0.2$), the most stable spin structure is found to be the coplanar inverse triangular spin structure, which is six-fold degenerate (labelled E-coplanar₆, following the notation in ref. [29]) and does not possess scalar spin chirality ($\chi = 0$, see Fig. 3(a)). Our theoretical results, therefore, are in accordance with prior experimental reports on bulk single crystals and epitaxial (0001) thin films [16–19, 23, 30]. Hence, the presence of in-plane DM interaction alone is not sufficient to induce scalar spin chirality in $\text{Mn}_3\text{Sn}/\text{Ta}$ heterostructures.

Next, we incorporate anisotropic strain, as observed in $\text{Mn}_3\text{Sn}/\text{Ta}$ heterostructures, where all three Mn-Mn bonds alter their lengths and become inequivalent reducing the symmetry of the Kagome triangles to C_1 (see Fig. 1(a)). To account for this we introduce factors α_{ij} , which renormalize the strength of interactions on each of the three bonds. Therefore, under anisotropic strain the

Hamiltonian can be written as:

$$H_{\Delta} = \alpha_{01}(J\mathbf{S}_0 \cdot \mathbf{S}_1 + \mathbf{D}_{01} \cdot (\mathbf{S}_0 \times \mathbf{S}_1)) + \alpha_{12}(J\mathbf{S}_1 \cdot \mathbf{S}_2 + \mathbf{D}_{12} \cdot (\mathbf{S}_1 \times \mathbf{S}_2)) + \alpha_{20}(J\mathbf{S}_2 \cdot \mathbf{S}_0 + \mathbf{D}_{20} \cdot (\mathbf{S}_2 \times \mathbf{S}_0)) + \frac{1}{2} \sum_i K(\hat{\mathbf{n}}_i \cdot \mathbf{S}_i)^2 \quad (3)$$

The factors α_{ij} are *a priori* unknown, which we will relate to the change in bond lengths, which are known. We assume here for simplicity that the Heisenberg and DM interactions are modified by the same factor. We do this by assuming that the exchange interactions are purely a function of the bond distance, i.e. for Heisenberg exchange $J = J(l)$ and

$$\alpha_{ij} = \frac{J(l_{ij})}{J(l_0)} \quad (4)$$

We then Taylor expand the function $J(l)$ around the unstrained bond length l_0 :

$$\begin{aligned} \alpha_{ij} &\approx \frac{J(l_0) + (l_{ij} - l_0) \left(\frac{dJ}{dl}\right)_{l=l_0}}{J(l_0)} = 1 + \frac{l_0}{J(l_0)} \left(\frac{dJ}{dl}\right)_{l=l_0} \left(\frac{l_{ij} - l_0}{l_0}\right) \\ &= 1 - \lambda \left(\frac{l_{ij} - l_0}{l_0}\right) \end{aligned} \quad (5)$$

where the dimensionless parameter $\lambda \equiv -\frac{l_0}{J(l_0)} \left(\frac{dJ}{dl}\right)_{l=l_0}$ expresses the sensitivity of the exchange interactions to small changes in bond length. A minus sign is included in the definition of λ because of the intuitive expectation that exchange interactions decrease with increasing l . Our calculations predict that anisotropic strain, parametrized by λ ($\lambda = 0$ corresponds to the unstrained case), stabilizes a non-coplanar ground state ($\chi \neq 0$) under any finite in-plane DM interaction, as shown in the phase diagram in Fig. 3(a). In such cases the ground state is two-fold degenerate and is denoted as E-noncoplanar₂. Following a recent neutron scattering experiment [30], which experimentally parametrized the exchange interactions in Mn_3Sn with small differences in bond length in the Kagome plane, we estimate $\lambda \approx -39$. This suggests that exchange interactions in Mn_3Sn can not only become stronger with increasing bond length ($\lambda < 0$) but the change can be quite large in magnitude. Representative non-coplanar magnetic ground states corresponding to both $\lambda = +39$ and $\lambda = -39$ with a net out-of-plane magnetic moment ($M_z \approx 9.3 m\mu_B/\text{Mn}$) similar to what is measured in our thin films, are shown in Fig. 3(b). For both the cases, the value of D_{\parallel}/J was tuned to reproduce the same out-of-plane magnetization, giving $D_{\parallel}/J = 0.14$ for $\lambda = 39$ and $D_{\parallel}/J = 0.19$ for $\lambda = -39$. We wish to emphasize that any non-zero λ , i.e. anisotropic strain in the Kagome lattice in presence of a finite in-plane DM interaction will stabilize a non-coplanar ground state, as is evident from the phase diagram presented in Fig. 3(a). We do not attempt a precise fit of the Hamiltonian parameters here, as it would be under-constrained, but the parameter sets used for calculations are illustrative of

the behavior across parameter space. Further details can be found in the Methods and in the Supplementary Information[22].

We incorporated the E-noncoplanar₂ magnetic structure shown in Fig. 3(b) in our first-principles calculations and calculated the resulting band structure. In Fig. 3(c), we present the band structure for the coplanar spin structure showing a nearly gapless nodal line along the $K-H$ line without any Berry curvature. Considering the non-coplanar spin configurations (E-noncoplanar₂), corresponding to $\lambda = +39$ and $\lambda = -39$, the nodal line becomes fully gapped (Fig. 3(d)). Importantly, E-noncoplanar₂ ground state breaks both the combined TM_z and the vertical glide mirror $\bar{M}_x = \{M_x|\frac{c}{2}\}$, which opens a large gap at nodal-band crossings. This results in a large Berry curvature Ω_{xy} , which is smeared out in energy and has a finite contribution at the Fermi energy, in agreement with our experimental observation of large AHC. The calculated value of σ_{xy}^z is 1.37 ($\lambda = +39$) and -0.71 ($\lambda = -39$) S/cm at the Fermi level, which goes up to 30 ($\lambda = +39$) and 31 ($\lambda = -39$) S/cm at 40 and 38meV below the Fermi level, respectively (see Fig. 3(e)). Notably, relaxing the magnetic structure in our DFT calculations, where substrate is not included, always chooses a coplanar magnetic configuration ($\chi = 0$) as the ground state, with a large difference in energy with any non-coplanar spin configuration ($\chi \neq 0$). This is in agreement with our theory calculations, which predicts a coplanar inverse triangular spin structure (E-coplanar₆) for all λ values when in-plane DM interaction (D_{\parallel}), which is induced by the inversion symmetry breaking at the heterointerface, is zero. Our work, therefore, underscores the importance of both in-plane DM interaction and anisotropic strain in stabilizing a non-coplanar ground state in the Kagome lattice. Moreover, for any finite anisotropic strain ($\lambda \neq 0$), a stronger DM interaction leads to an enhanced out-of-plane spin canting (see Fig. 3(a)), which is expected to result in a larger Berry curvature contribution. This is also borne out in our experiments. Samples which are capped with Ta shows a larger out-of-plane spin canting and AHC (see Fig. 2(b),(d)), where DM interaction strength is expected to be stronger due to an additional Mn₃Sn/Ta hetero-interface.

D. Thermal assisted electrical switching of anomalous Hall effect and realization of multiple-stable memory states

Having understood the origin of anomalous Hall effect in Mn₃Sn(0001)/Ta heterostructures, we now investigate the possibility of switching the non-coplanar magnetic order with electric current. Electrical switching of the coplanar inverse triangular spin structure leading to a reversal of sign of the AHE in Mn₃Sn has already been reported, where the Mn spins rotates within the Kagome plane [31–33]. The non-collinear inverse triangular spin configuration of Mn₃Sn has been shown to have clus-

ter magnetic octupole as the order parameter [34]. It has been claimed that spin-orbit torque (SOT) from an adjacent heavy-metal layer under the application of an in-plane magnetic field can deterministically switch the direction of the octupole moment, similar to spin-orbit torque switching of magnetization in a ferromagnet [35–37], which in turn results in the switching of the AHE [31, 32]. However, recent reports suggest a possible role of thermally driven demagnetization on application of charge current in seeding the antiferromagnetic order at the interface under a spin-orbit field [38, 39].

In our thin films not only the magnetic ground state is different, as already discussed, so is its switching behavior under the application of electric pulse. Although Ta layer in Mn₃Sn/Ta can generate appreciable spin current, we did not observe any evidence of spin-orbit torque driven switching behavior in our thin films. In contrast to expectation from switching by a spin-orbit field, the electrically induced switching in our case depends only on the magnitude, but not on the sign of the applied current. Furthermore, in our case, deterministic switching of anomalous Hall effect was observed under a tiny bias magnetic field applied perpendicular to the Kagome plane. Dependence of the observed switching behavior on both current pulse amplitude and pulse width is shown in Fig. 4. In both the cases, switching was observed only when the transient temperature of the device went above the Neel temperature of Mn₃Sn ($T_N \approx 420$ K), which clearly establishes that it is driven by thermal effects. Under an applied electric pulse, the sample undergoes demagnetization as the temperature rises above the Neel temperature. A small but a finite cooling field lifts the two-fold degeneracy of E-noncoplanar₂ magnetic ground state and sets the net magnetization of the nucleated domains along the direction of the field. This in turn results in a switching of the sign of AHE on reversing the direction of the cooling field. Due to the two-fold degeneracy of the E-noncoplanar₂ ground state, applying an electric pulse in zero magnetic field leads to the formation of magnetic domains with equal net magnetization along the +z and -z directions after demagnetization. In such cases, the net anomalous Hall effect in the sample cancels out to zero, as observed in our experiment (see Fig. 4(a)). Further details are provided in the Methods and in the Supplementary Information [22]. The unique magnetic ground state and thermally driven switching behavior in anisotropic strained Mn₃Sn/Ta thin film heterostructures allows access to a number of different non-volatile anomalous Hall resistance(AHR) states, which correspond to different domain configurations. Such AHR states can be accessed by the application of electrical pulse under different bias fields, as shown in Fig. 5. A symmetry-breaking bias field of ≈ 0.13 Tesla is found to be sufficient for Ta/Mn₃Sn/Ta/AlO_x heterostructures to completely saturate the domain structure. At saturation the out-of-plane magnetization (M_z) of all the domains are aligned along the applied bias field that results in a full switching of the AHE on application of current. Similar behavior is

also observed in Ta/Mn₃Sn/AlO_x heterostructures [22]. Application of different bias fields, which are less than the saturation field, stabilizes unique domain structure post electric pulse driven demagnetization in Mn₃Sn. Under those conditions the proportion of domains aligned along +z and -z directions depends on the applied bias field during the switching process and results in the observation of different anomalous Hall resistances. This allows us to achieve multiple AHR memory states in Mn₃Sn that are tunable by electric current. Moreover, the change in AHR is linear over a wide magnetic bias field range of ± 200 Oe as shown in Fig. 5(b). The switching behavior is symmetric with respect to the polarity of the bias field, as evidenced from the resistance loops shown in Fig. 5(c). The resistance loops at different bias fields are obtained as follows: (i) At first, an electric pulse is applied at a positive bias field. (ii) Then, the bias field is reversed (iii) The same electric pulse is applied at a reversed bias field, which reverses the sign of AHR (R_{xy}). (iv) The applied field is reversed again bringing it back to its original value. (v) Application of electric pulse brings the AHR to its starting point. The AHR retraces the same resistance loop on repetition of these five steps indicating the stability of the switching process. The AHR memory states are also fairly stable against magnetic field fluctuations. Once a particular memory state is achieved, we show the evolution of such a state under the application of magnetic field in Fig. 5(d). We choose the criterion for field stability as the field range over which the resistance stays within 2% of the full range ($\Delta R_{xy} = 0.21 \times 2/100 = 0.0042 \Omega$), which allows us to define 50 unique AHR memory states. We find that all such states are stable within a field range of at least ≈ 1769 Oe, indicative of good resilience against field fluctuations. The estimated current density required for switching the AHE in Mn₃Sn in both Ta/Mn₃Sn/AlO_x and Ta/Mn₃Sn/Ta/AlO_x heterostructures is $\approx 1.5 \times 10^{10}$ A/m², which is an order of magnitude lower than spin-orbit torque switching of magnetic octupole in Mn₃Sn thin films [32] and spin-orbit torque driven switching in typical ferromagnets. Distinct switching behavior in Mn₃Sn/Ta heterostructures provides additional evidence for the stabilization of non-coplanar magnetic ground state in this system.

III. CONCLUSION

In summary, we demonstrated that anisotropic strain and in-plane interfacial DM interaction enable the imprinting of scalar spin chirality in the magnetic ground state of a Kagome lattice. This leads to significant Berry curvature effects from gapped nodal lines in momentum space, resulting in a pronounced AHE in the Kagome plane at room temperature. Furthermore, we have showed that applying an electric pulse can induce thermally assisted switching of the AHE, allowing access to multiple non-volatile, field-stable AHR memory states - an uncommon feature in antiferromagnets. Coupled

with the large AHE at room temperature, this new functionality positions Kagome antiferromagnets as promising candidates for spintronic and neuromorphic computing applications. Additionally, finite scalar spin chirality may stabilize non-trivial chiral ground states, including skyrmion phases, which will be explored in future research. While our results were demonstrated in the prototypical system of Mn₃Sn, these concepts should be applicable to other Kagome lattice systems where thin film engineering techniques such as anisotropic strain and inversion symmetry breaking can be employed to stabilize non-trivial magnetic ground states.

Acknowledgments

We thank Devendra Buddhikot, Ganesh Jangam, and Bhagyashree Chalke for technical assistance. We acknowledge the Department of Science and Technology (DST), SERB grant SRG/2021/000414 and Department of Atomic Energy (DAE) of the Government of India (12-R&D-TFR-5.10-0100) for support. We thank Dr. Sunil Ojha and Dr. G. R. Umamathy for Rutherford backscattering spectrometry (RBS) measurements on Mn₃Sn thin films at Inter-University Accelerator Centre (IUAC), Delhi. We also acknowledge the use of the laser writing facility at National Nano Fabrication Centre (NNFC), IISc.

Author Contributions

D.P. and S.Y. contributed equally to this work. S.C. conceived the project and was responsible for its overall execution. S.C., D.P., and S.Y. planned the experiments. D.P. with assistance from N.K., D.M., S.S., and S.G. fabricated the thin films and performed structural characterization. B.Sat. prepared the thin film lamellae and performed TEM characterization. D.P. and S.Y. fabricated the Hall bar devices. S.Y. and D.P. with assistance from S.G. and S.K.S. performed the electrical and magnetometry measurements. D.P., with assistance from S.Y., N.K., K.G., S.K.S., S.S. and S.C., analyzed the data. O.B. performed the numerical calculations. B.P. and B.S. performed the ab-initio calculations. O.B., B.P., and B.S. provided theoretical explanation. D.P. and S.C. wrote the manuscript with inputs from O.B., B.P., and B.S. All authors discussed the results and commented on the manuscript.

Data Availability

The data that supports the findings of this study are available from the corresponding author upon reasonable request.

Competing Interests

The authors declare no competing interests.

Materials and Methods

A. Thin film preparation and characterization

High purity targets of Mn (99.99%) & Sn (99.99%) were co-sputtered using RF magnetron sputtering to synthesize epitaxial thin film of Mn_3Sn . Before deposition of Mn_3Sn , Ta was sputtered at 600°C on epitaxial grade *c*-plane sapphire substrates using RF magnetron sputtering in the same chamber at a 10 mTorr pressure followed by an annealing period of 10 mins at the same temperature. The sample was subsequently cooled to 300°C temperature to synthesize Mn_3Sn films at a growth rate of ≈ 1.25 Å/s. Following which either an AlO_x or Ta(11 nm)/ AlO_x protective capping layer was deposited on the sample at room temperature to prevent it from oxidation. Lastly, an *in situ* post-annealing treatment of one-hour duration was performed at 450°C with a slow cooling rate of $\approx 1.5^\circ\text{C}$ per minute. The high-temperature post-annealing step was found to be essential for the realization Mn_3Sn thin films of good structural and phase quality. Rutherford backscattering spectrometry (RBS) was used to examine the stoichiometry of Mn_3Sn in thin film heterostructures. The measurements were done using 2MeV alpha particles at the RBS beamline (Pelletron Accelerator RBS-AMS Systems (PARAS)) at Inter-University Accelerator Centre (IUAC), Delhi. The fits to the obtained data were performed using RUMP software.

The crystal structure of thin film heterostructures was evaluated using x-ray diffraction (XRD) and high-resolution transmission electron microscopy (HR-TEM). XRD data was collected using a Rigaku SmartLab X-ray diffractometer with a 9 kW rotating anode with Cu $K\alpha$ radiation. Cross-sectional TEM samples were prepared using conventional mechanical thinning followed by Ar ion milling using precision ion polishing system (PIPS, GATAN Inc.) at an energy of 4.0 keV and cleaning at 1.5 keV. HR-TEM images were taken using a FEI Tecnai G2 F30-ST microscope operated at 300 keV.

B. Magnetotransport and electrical switching measurements

For magnetotransport and electrical switching measurements, Hall bars of width $50\mu\text{m}$ were fabricated us-

ing standard optical photolithography techniques. The Hall resistivity and the magnetoresistance were measured in a commercial PPMS (Quantum Design) using low-frequency a.c. lock-in technique. For the switching measurements, the electrical pulses were applied using a Keithley 6221 current source, where the Hall voltage before and after the application of the pulse was measured using a Keithley 2182A nanovoltmeter. The transient longitudinal voltage was collected using a fast NI-DAQ-6210 with a sampling rate 250KS/s, from where transient temperature during the application of pulse was estimated [22]. The magnetometry measurements were performed in a commercial SQUID-VSM magnetometer (Quantum Design).

C. Theory calculations

The effect of strain and DM interaction on the spin configuration of Mn_3Sn was calculated in a classical approximation, where the $S = 3/2$ moments are treated as classical vectors of fixed length. The Hamiltonian is given as a sum over kagome triangles as described in eqns. 1 and 2. For such a Hamiltonian, the classical energy is known to be minimized by translationally invariant states [29], so it is sufficient to minimize the energy on a single triangle and then tile the resulting configuration over the whole system. Optimal configurations on a single triangle were found by numerically minimizing H_Δ with respect to the spin directions $\mathbf{S}_{0,1,2}$, shown in Fig. 3(b).

First-principles calculations were performed within the framework of density functional theory using the projector augmented wave potential with the Vienna Ab initio Simulation Package (VASP) [40, 41]. Generalized gradient approximation with the Perdew-Burke-Ernzerhof parametrization [42] was used to include exchange-correlation effects. The self-consistent relativistic calculations were performed with a plane wave cutoff energy of 400 eV and a Γ centered $10 \times 10 \times 12$ k-mesh for Brillouin zone sampling. Material-specific tight-binding Hamiltonian was constructed by generating Wannier functions derived from Mn-*s*, *d*, and Sn-*p* states [43]. The anomalous Hall conductivities were calculated using a dense $350 \times 350 \times 350$ points grid with the WannierBerry code [44].

[1] Y. Wang, H. Wu, G. T. McCandless, J. Y. Chan, M. N. Ali, Quantum states and intertwining phases in kagome

materials. *Nat. Rev. Phys.* **5**, 635 (2023)

[2] Q. Wang, H. Lei, Y. Qi, C. Felser, Topological Quantum

- Materials with Kagome Lattice. *Acc. Mater. Res.* **5**, 786 (2024)
- [3] L. Ye, M. Kang, J. Liu, F. von Cube, C. R. Wicker, T. Suzuki, C. Jozwiak, A. Bostwick, E. Rotenberg, D. C. Bell, L. Fu, R. Comin, J. G. Checkelsky, Massive Dirac fermions in a ferromagnetic kagome metal. *Nature* **555**, 638 (2018)
- [4] M. Kang, L. Ye, S. Fang, J.-S. You, A. Levitan, M. Han, J. I. Facio, C. Jozwiak, A. Bostwick, E. Rotenberg, M. K. Chan, R. D. McDonald, D. Graf, K. Kaznatcheev, E. Vescovo, D. C. Bell, E. Kaxiras, J. v. d. Brink, M. Richter, M. P. Ghimire, J. G. Checkelsky, R. Comin, Dirac fermions and flat bands in the ideal kagome metal FeSn. *Nat. Mater.* **19**, 163 (2020)
- [5] M. Kang, S. Fang, L. Ye, H. C. Po, J. Denlinger, C. Jozwiak, A. Bostwick, E. Rotenberg, E. Kaxiras, J. G. Checkelsky, R. Comin, Topological flat bands in frustrated kagome lattice CoSn, *Nat. Commun.* **11**, 4004 (2020)
- [6] H. Yang, Y. Sun, Y. Zhang, W.-J. Shi, S. S P Parkin, B. Yan, Topological Weyl semimetals in the chiral antiferromagnetic materials Mn₃Ge and Mn₃Sn, *New J. Phys.* **19**, 015008 (2017)
- [7] J. Kübler, C. Felser, Weyl fermions in antiferromagnetic Mn₃Sn and Mn₃Ge. *EPL* **120**, 47002 (2018)
- [8] K. Kuroda, T. Tomita, M.-T. Suzuki, C. Bareille, A. A. Nugroho, P. Goswami, M. Ochi, M. Ikhlas, M. Nakayama, S. Akebi, R. Noguchi, R. Ishii, N. Inami, K. Ono, H. Kumigashira, A. Varykhalov, T. Muro, T. Koretsune, R. Arita, S. Shin, Takeshi Kondo, S. Nakatsuji, Evidence for magnetic Weyl fermions in a correlated metal. *Nat. Mater.* **16**, 1090 (2017)
- [9] T. Chen, T. Tomita, S. Minami, M. Fu, T. Koretsune, M. Kitatani, I. Muhammad, D. N.-Hamane, R. Ishii, F. Ishii, R. Arita, S. Nakatsuji, Anomalous transport due to Weyl fermions in the chiral antiferromagnets Mn₃X, X = Sn, Ge. *Nat. Commun.* **12**, 572 (2021)
- [10] H. Ohmori, S. Tomiyoshi, H. Yamauchi, H. Yamamoto, Spin structure and weak ferromagnetism of Mn₃Sn. *J. Magn. Mater.* **70**, 249 (1987)
- [11] S. Tomiyoshi, Y. Yamaguchi, Magnetic Structure and Weak Ferromagnetism of Mn₃Sn Studied by Polarized Neutron Diffraction. *J. Phys. Soc. Jpn.* **51**, 2478 (1982)
- [12] P. J. Brown, V. Nunez, F. Tasset, J. B. Forsyth, P. Radhakrishna, Determination of the magnetic structure of Mn₃Sn using generalized neutron polarization analysis. *J. Phys.: Condens. Matter* **2**, 9409 (1990)
- [13] E. Krén, J. Paitz, G. Zimmer, E. Zsoldos, Study of the magnetic phase transformation in the Mn₃Sn phase. *Physica B+C* **80**, 226 (1975)
- [14] T. Nagamiya, S. Tomiyoshi, Y. Yamaguchi, Triangular spin configuration and weak ferromagnetism of Mn₃Sn and Mn₃Ge. *Solid State Commun.* **42**, 385 (1982)
- [15] L. M. Sandratskii, J. Kübler, Role of Orbital Polarization in Weak Ferromagnetism. *Phys. Rev. Lett.* **76**, 4963 (1996)
- [16] S. Nakatsuji, N. Kiyohara, T. Higo, Large anomalous Hall effect in a non-collinear antiferromagnet at room temperature. *Nature* **527**, 212 (2015)
- [17] X. Li, J. Koo, Z. Zhu, K. Behnia, B. Yan, Field-linear anomalous Hall effect and Berry curvature induced by spin chirality in the kagome antiferromagnet Mn₃Sn. *Nat. Commun.* **14** 1642 (2023)
- [18] T. Ikeda, M. Tsunoda, M. Oogane, S. Oh, T. Morita, Y. Ando, Fabrication and evaluation of highly c-plane oriented Mn₃Sn thin films. *AIP Advances* **10**, 015310 (2020)
- [19] J. M. Taylor, A. Markou, E. Lesne, P. K. Sivakumar, C. Luo, F. Radu, P. Werner, C. Felser, S. S. P. Parkin, Anomalous and topological Hall effects in epitaxial thin films of the noncollinear antiferromagnet Mn₃Sn. *Phys. Rev. B* **101**, 094404 (2020)
- [20] S. G. Jones, N. Materise, K. W. Leung, J. C. Weber, B. D. Isakov, X. Chen, J. Zheng, A. Gyenis, B. Jaeck, C. R. H. McRae, Grain size in low loss superconducting Ta thin films on c axis sapphire. *J. Appl. Phys.* **134**, 144402 (2023)
- [21] L. D. Alegria, D. M. Tennant, K. R. Chaves, J. R. I. Lee, S. R. O'Kelley, Y. J. Rosen, J. L. DuBois, Two-level systems in nucleated and non-nucleated epitaxial alpha-tantalum films. *Appl. Phys. Lett.* **123**, 062601 (2023)
- [22] see Supplementary Information.
- [23] N. H. Sung, F. Ronning, J. D. Thompson, E. D. Bauer, Magnetic phase dependence of the anomalous Hall effect in Mn₃Sn single crystals. *Appl. Phys. Lett.* **112**, 132406 (2018)
- [24] I. Dzyaloshinsky, A Thermodynamic Theory of Weak Ferromagnetism of Antiferromagnetics. *J. Phys. Chem. Solids* **4**, 241 (1958).
- [25] T. Moriya, Anisotropic Superexchange Interaction and Weak Ferromagnetism. *Phys. Rev.* **120**, 91 (1960)
- [26] H. Yang, A. Thiaville, S. Rohart, A. Fert, M. Chshiev, Anatomy of Dzyaloshinskii-Moriya Interaction at Co/Pt Interfaces. *Phys. Rev. Lett.* **115**, 267210 (2015)
- [27] H. Tsai, T. Higo, K. Kondou, S. Sakamoto, A. Kobayashi, T. Matsuo, S. Miwa, Y. Otani, S. Nakatsuji, Large Hall Signal due to Electrical Switching of an Antiferromagnetic Weyl Semimetal State. *Small Sci.* **1**, 2000025 (2021)
- [28] J. Liu, L. Balents, Anomalous Hall Effect and Topological Defects in Antiferromagnetic Weyl Semimetals: Mn₃Sn/Ge. *Phys. Rev. Lett.* **119**, 087202 (2017)
- [29] O. Benton, Ordered ground states of kagome magnets with generic exchange anisotropy. *Phys. Rev. B* **103**, 174425 (2021)
- [30] P. Park, J. Oh, K. Uhlířová, J. Jackson, A. Deák, L. Szunyogh, K. H. Lee, H. Cho, H.-L. Kim, H. C. Walker, D. Adroja, V. Sechovsky, J-G. Park, Magnetic excitations in non-collinear antiferromagnetic Weyl semimetal Mn₃Sn. *npj Quantum Materials* **3**, 63 (2018)
- [31] H. Tsai, T. Higo, K. Kondou, T. Nomoto, A. Sakai, A. Kobayashi, T. Nakano, K. Yakushiji, R. Arita, S. Miwa, Y. Otani, S. Nakatsuji, Electrical manipulation of a topological antiferromagnetic state. *Nature* **580**, 608 (2020)
- [32] T. Higo, K. Kondou, T. Nomoto, M. Shiga, S. Sakamoto, X. Chen, D. N.-Hamane, R. Arita, Y. Otani, S. Miwa, S. Nakatsuji, Perpendicular full switching of chiral antiferromagnetic order by current. *Nature* **607**, 474 (2022)
- [33] Y. Takeuchi, Y. Yamane, J. Y. Yoon, R. Itoh, B. Jinnai, S. Kanai, J. Ieda, S. Fukami, H. Ohno, Chiral spin rotation of non-collinear antiferromagnet by spin-orbit torque. *Nat. Mater.* **20**, 1364 (2021)
- [34] M.-T. Suzuki, T. Koretsune, M. Ochi, and R. Arita, Cluster multipole theory for anomalous Hall effect in antiferromagnets. *Phys. Rev. B* **95**, 094406 (2017)
- [35] A. Manchon, J. Železný, I. M. Miron, T. Jungwirth, J. Sinova, A. Thiaville, K. Garello, P. Gambardella, Current-induced spin-orbit torques in ferromagnetic and antiferromagnetic systems. *Rev. Mod. Phys.* **91**, 035004

- (2019)
- [36] A. Chernyshov, M. Overby, X. Liu, J. K. Furdyna, Y. L. Geller, L. P. Rokhinson, Evidence for reversible control of magnetization in a ferromagnetic material by means of spin-orbit magnetic field. *Nat. Phys.* **5**, 656 (2009)
- [37] I. M. Miron, G. Gaudin, S. Auffret, B. Rodmacq, A. Schuhl, S. Pizzini, J. Vogel, P. Gambardella, Current-driven spin torque induced by the Rashba effect in a ferromagnetic metal layer. *Nat. Mater.* **9**, 230 (2010)
- [38] B. Pal, B. K. Hazra, B. Göbel, J.-C. Jeon, A. K. Pandeya, A. Chakraborty, O. Busch, A. K. Srivastava, H. Deniz, J. M. Taylor, H. Meyerheim, I. Mertig, S.-H. Yang, S. S. P. Parkin, Setting of the magnetic structure of chiral kagome antiferromagnets by a seeded spin-orbit torque. *Sci. Adv.* **8**, eabo5930 (2022)
- [39] G. K. Krishnaswamy, G. Sala, B. Jacot, C.-H. Lambert, R. Schlitz, M. D. Rossell, P. Noël, P. Gambardella, Time-Dependent Multistate Switching of Topological Antiferromagnetic Order in Mn_3Sn . *Phys. Rev. Applied* **18**, 024064 (2022)
- [40] G. Kresse, J. Furthmüller, Efficient iterative schemes for ab initio total-energy calculations using a plane-wave basis set. *Phys. Rev. B* **54**, 11169 (1996)
- [41] G. Kresse, D. Joubert, From ultrasoft pseudopotentials to the projector augmented-wave method. *Phys. Rev. B* **59**, 1758 (1999)
- [42] J. P. Perdew, K. Burke, M. Ernzerhof, Generalized Gradient Approximation Made Simple. *Phys. Rev. Lett.* **77**, 3865 (1996)
- [43] A. A. Mostofia, J. R. Yatesb, G. Pizzif, Y.-S. Leec, I. Souzad, D. Vanderbilte, N. Marzarif, An updated version of wannier90: A tool for obtaining maximally-localised Wannier functions. *Comput. Phys. Commun.* **185**, 2309 (2014)
- [44] S. S. Tsirkin, High performance Wannier interpolation of Berry curvature and related quantities with Wannier-Berri code. *npj Comput. Mater.* **7**, 33 (2021)

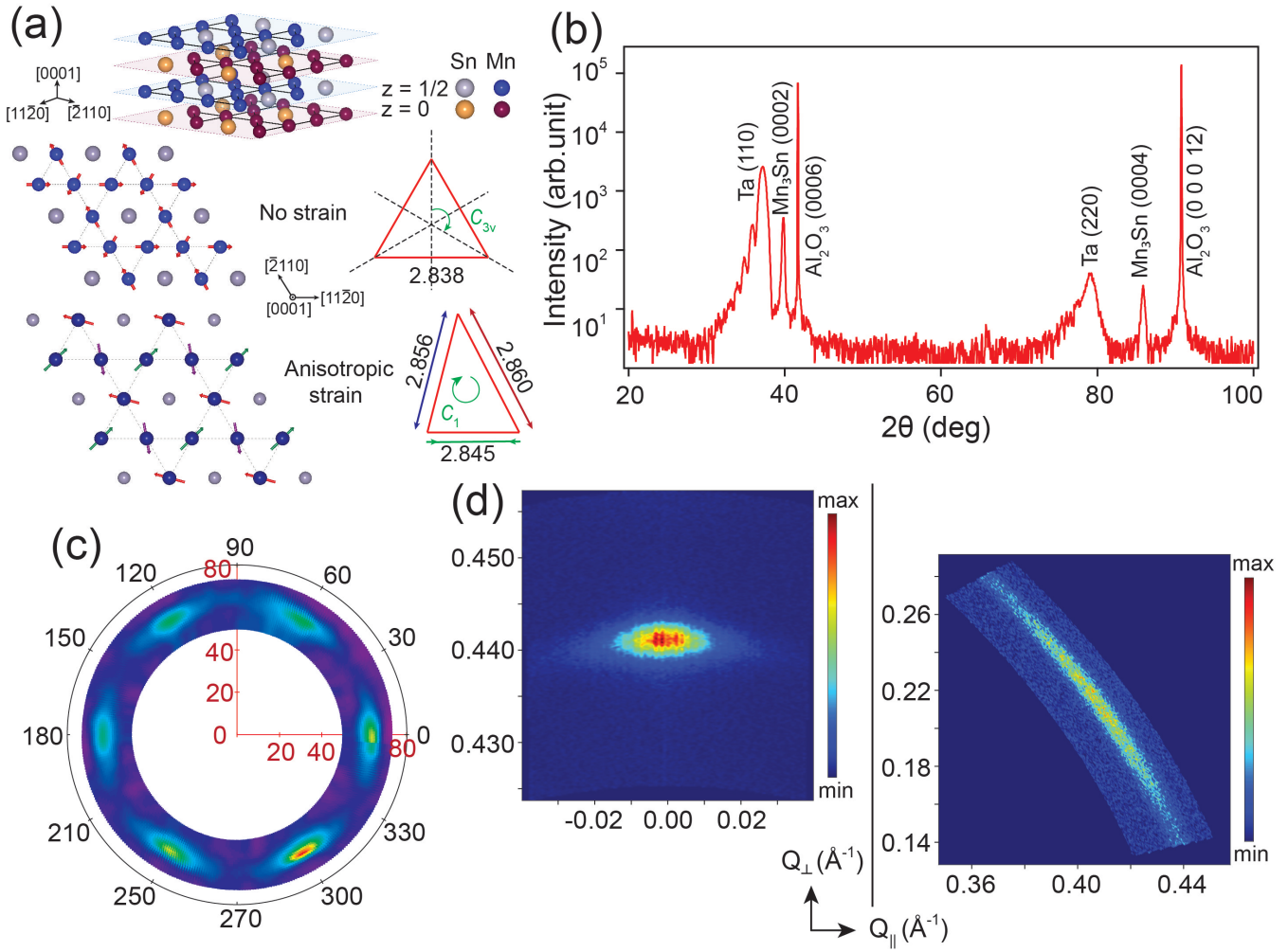


Figure 1: **Anisotropic strain in $\text{Mn}_3\text{Sn}/\text{Ta}$ heterostructures.** (a) Three-dimensional crystal structure of Mn_3Sn , which consists of bilayer (AB) stacking of Kagome planes. Top view of the Kagome plane without and with anisotropic strain that has C_{3v} and C_1 point group symmetry of the Kagome triangles, respectively. (b) Out-of-plane θ - 2θ XRD scan of $\text{Mn}_3\text{Sn}/\text{Ta}$ heterostructures (c) Pole figure plot of Mn_3Sn $\{20\bar{2}1\}$ family of diffraction peaks showing a six-fold symmetry, establishing the epitaxial nature of Mn_3Sn . (d) RSM plots of (0002) and $(20\bar{2}1)$ Bragg peaks. The in-plane lattice parameters are estimated by measuring the q vectors of the $\{20\bar{2}1\}$ family of Bragg peaks[22].

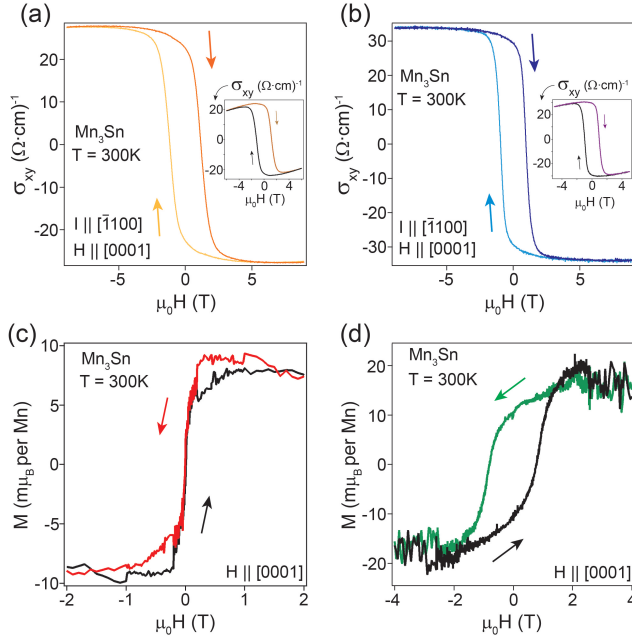


Figure 2: **Anomalous Hall effect in Mn₃Sn/Ta heterostructures.** Anomalous Hall conductivity at 300K of (a) Ta(11nm)/ Mn₃Sn(90nm)/ AlO_x(8nm) and (b) Ta(11nm)/ Mn₃Sn(90nm)/ Ta(11nm)/ AlO_x(8nm) thin film heterostructures synthesized on c-plane sapphire substrates. The arrows indicate the direction of magnetic field sweeps, which is applied perpendicular to the Kagome plane (along [0001]) and the current is applied along $[\bar{1}100]$. Insets show corresponding Hall conductivity as a function of magnetic field. Magnetization as a function of magnetic field at 300K for (c) Ta(11nm)/ Mn₃Sn(90nm)/ AlO_x(8nm) and (d) Ta(11nm)/ Mn₃Sn(90nm)/ Ta(11nm)/ AlO_x(8nm) thin film heterostructures with the magnetic field applied perpendicular to the Kagome plane. A linear diamagnetic background has been subtracted in both the cases.

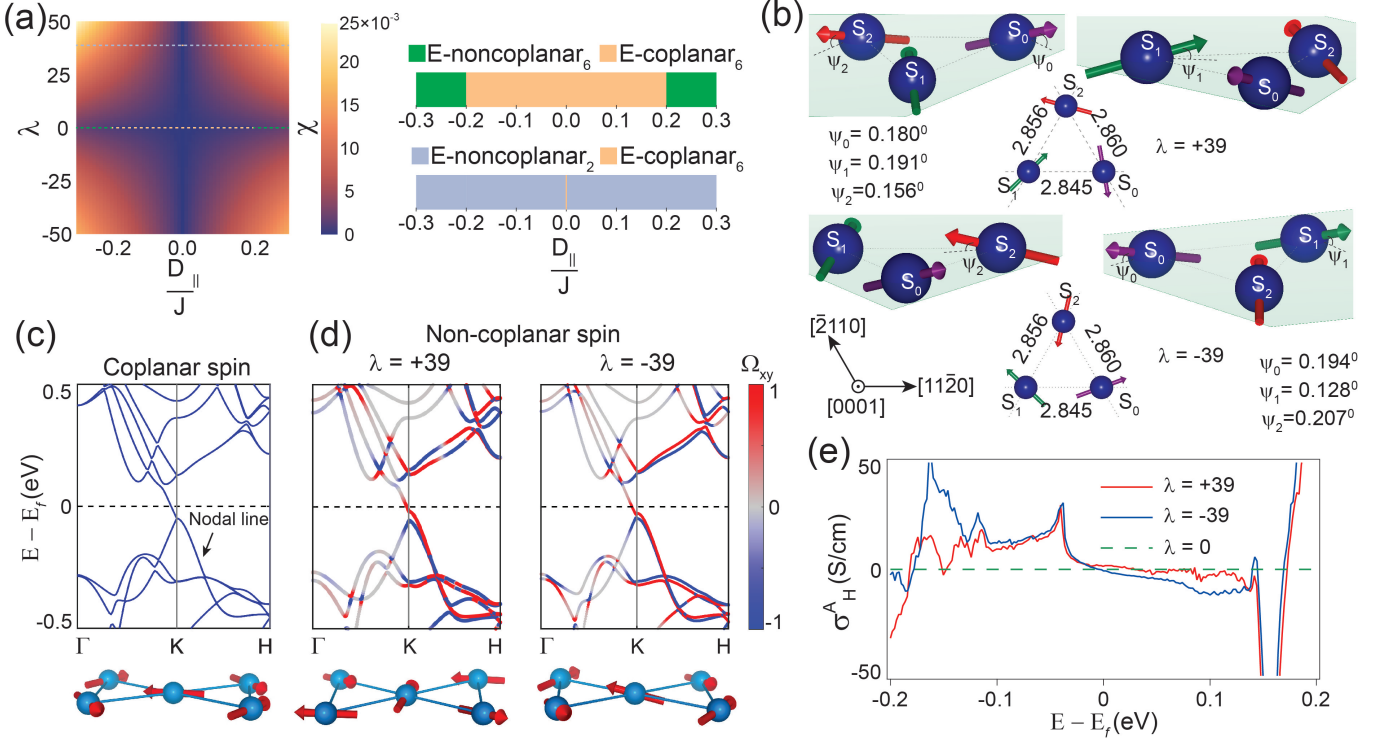


Figure 3: **Non-coplanar spin structure in Mn₃Sn/Ta heterostructures.** (a) Phase diagram of the magnetic ground state as a function of anisotropic strain and in-plane DM interaction. Scalar spin chirality(χ) of the magnetic ground state as a function of λ and D_{\parallel}/J (all parameters defined in the text). Phase diagram as a function of D_{\parallel}/J is shown for two specific λ values viz. $\lambda = 0$, and $\lambda = +39$. (b) Illustration of non-coplanar magnetic ground states (E-noncoplanar₂) having an out-of-plane magnetic moment of $M_z \approx 9.3 \text{ m}\mu\text{B}/\text{Mn}$ corresponding to $\lambda = +39$ and $\lambda = -39$, as described in the text. Band structure obtained with (c) coplanar inverse triangular spin structure (E-coplanar₆, $\lambda = 0$) and (d) non-coplanar (E-noncoplanar₂) spin configurations corresponding to $\lambda = +39$ and $\lambda = -39$, as shown in (b). The bottom panels show the spin-configurations and the color bar represents the Berry curvature Ω_{xy} . (e) Calculated anomalous Hall conductivities as a function of binding energy for $\lambda = 0, +39$, and -39 .

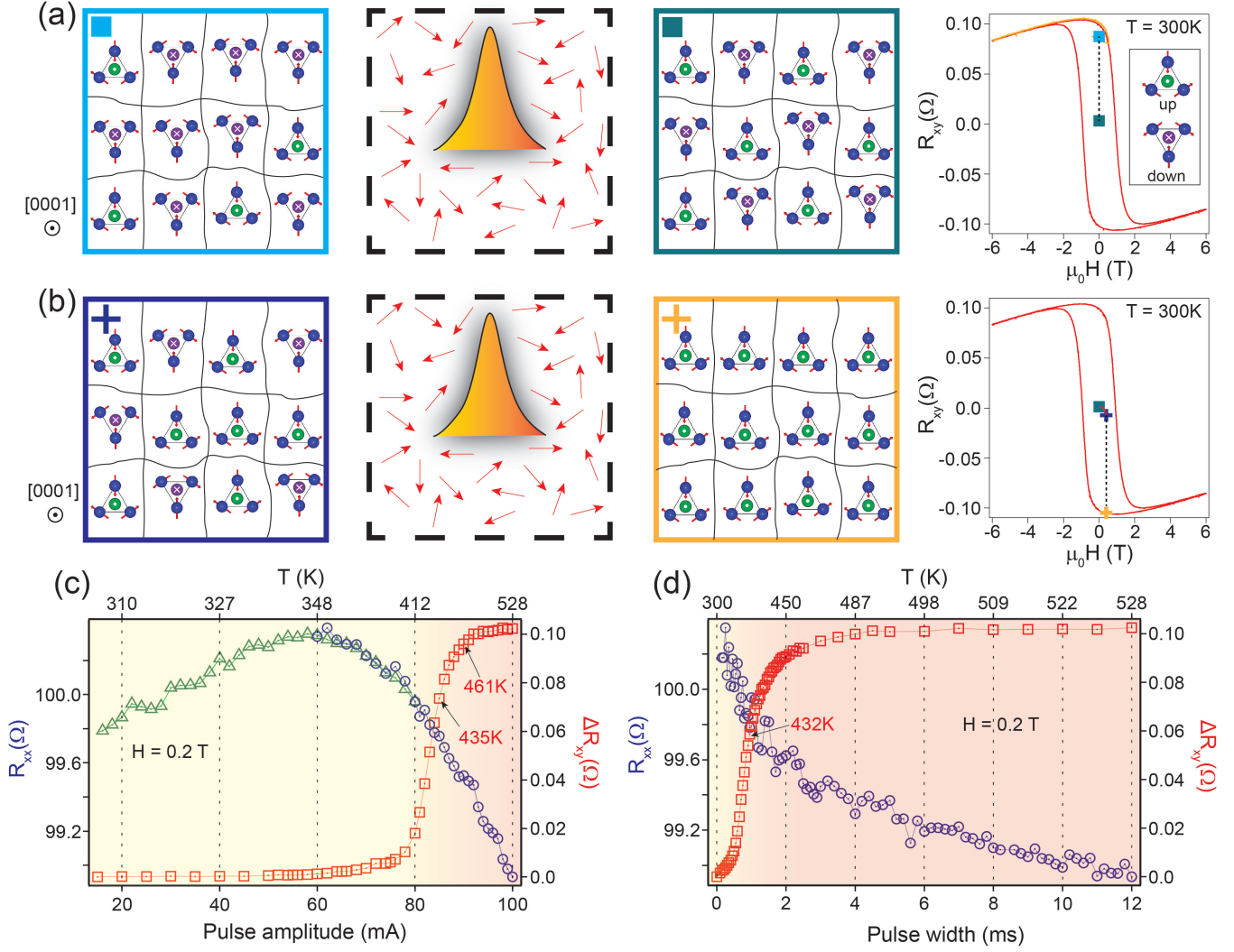


Figure 4: **Thermal assisted switching of anomalous Hall effect in Mn_3Sn .** Switching of anomalous Hall resistance (a) under zero magnetic field. (b) under a finite magnetic field of $+0.2\text{ T}$ in $\text{Ta}(11\text{nm})/\text{Mn}_3\text{Sn}(90\text{nm})/\text{Ta}(11\text{nm})/\text{AlO}_x(8\text{nm})$ heterostructures. Under a zero magnetic field, post demagnetization due to the current pulse, domains with both “up” and “down” magnetization nucleate in equal proportions, resulting in zero anomalous Hall resistance. In contrast, when a finite cooling field of $+0.2\text{ T}$ is applied, all domains align in the “up” direction, leading to a significant anomalous Hall resistance. Switching behavior as a function of (c) pulse amplitude with the pulse width fixed at 12 ms and (d) pulse width with the pulse amplitude fixed at 100 mA . The transient temperature during the application of pulse is estimated by measuring the longitudinal resistance (R_{xx}) [22]. R_{xx} is measured directly by an NI-DAQ device for low voltages, shown in green, and through a divider circuit for higher voltages, shown in blue. Switching measurements are performed under a bias field of $+0.2\text{ T}$.

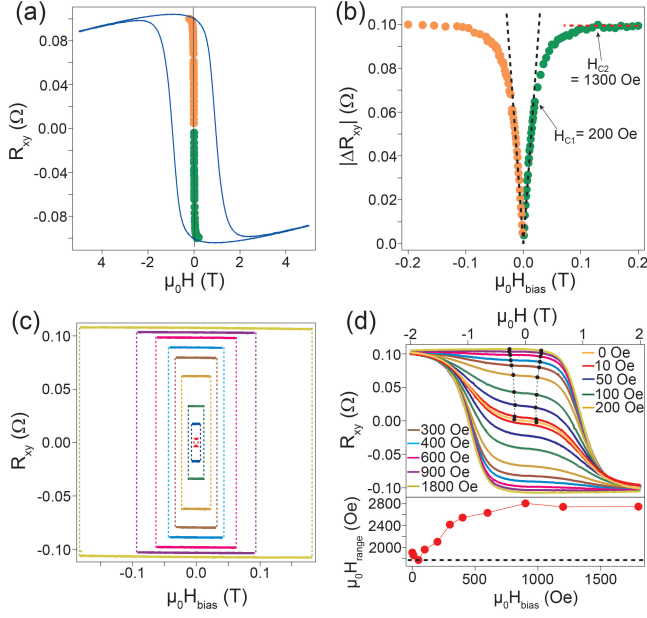


Figure 5: Multiple-stable anomalous Hall resistance memory states in Mn_3Sn . (a) Anomalous Hall resistance (R_{xy}) states after application of electrical pulse under different bias fields in Ta(11nm)/ Mn_3Sn (90nm)/ Ta(11nm)/ AlO_x (8nm) heterostructures. Results with positive and negative bias fields are shown in green and orange, respectively. The hysteresis curve of the AHE as a function of magnetic field is shown in blue for reference. (b) The change in R_{xy} due to electrical switching under a bias field w.r.t the initial state. The initial state is obtained by applying an electric pulse with zero bias field that brings R_{xy} to zero (see discussion in the text). The black dashed lines are linear fits. The red dashed line in (b) shows saturation behavior for fields above 1300 Oe. (c) Symmetrical switching behavior for positive and negative bias fields shown for different magnitudes of the bias field. (d) Evolution of the AHR memory states with magnetic field. The field range over which the AHR remains within $\pm 0.0021\Omega$ of its value at zero field (see text) is shown with a black dot-dash line. The estimated stability field ranges as a function of bias fields is shown at the bottom. The dashed line in black corresponds to 1769 Oe, the minimum value obtained for the field range. In all cases, a single pulse of 100mA and of duration 12ms is applied for electrical switching.